Geophysical Research Letters

RESEARCH LETTER
10.1029/2020GL091453

Key Points:
- Mesospheric winds from multiple longitudes in the NH are combined to diagnose zonal wave numbers of waves during the Antarctic SSW 2019
- Diagnosed are Q6DW, Q10DW, M2, SW1, SW2, SW3, and LSB and USB of Q10DW-SW2 nonlinear interactions
- LSB and USB are generated asynchronously, during which their parent waves evolve following the Manley-Rowe energy relations

Supporting Information:
- Supporting Information S1

Correspondence to:
M. He,
he@iap-kborn.de

Citation:
He, M., Chau, J. L., Forbes, J. M., Thorsen, D., Li, G., Siddiqui, T. A., et al. (2020). Quasi-10-day wave and semidiurnal tide nonlinear interactions during the Southern Hemispheric SSW 2019 observed in the Northern Hemispheric mesosphere. *Geophysical Research Letters*, *47*, e2020GL091453. https://doi.org/10.1029/2020GL091453

Received 27 OCT 2020
Accepted 3 NOV 2020
Accepted article online 20 NOV 2020

Quasi-10-Day Wave and Semidiurnal Tide Nonlinear Interactions During the Southern Hemispheric SSW 2019 Observed in the Northern Hemispheric Mesosphere

Maosheng He[1], Jorge L. Chau[1], Jeffrey M. Forbes[2], Denise Thorsen[3], Guozhu Li[4,5], Tarique Adnan Siddiqui[1], Yosuke Yamazaki[6], and Wayne K. Hocking[7]

[1]Leibniz-Institute of Atmospheric Physics at the Rostock University, Kühlungsborn, Germany, [2]Ann and H.J. Smead Department of Aerospace Engineering Sciences, University of Colorado, Boulder, CO, USA, [3]Department of Electrical and Computer Engineering, University of Alaska Fairbanks, Fairbanks, AK, USA, [4]Beijing National Observatory of Space Environment, Institute of Geology and Geophysics, Chinese Academy of Sciences, Beijing, China, [5]College of Earth and Planetary Sciences, University of Chinese Academy of Sciences, Beijing, China, [6]GFZ German Research Centre for Geosciences, Potsdam, Germany, [7]University of Western Ontario, Richmond, Ontario, Canada

Abstract Mesospheric winds from three longitudinal sectors at 65°N and 54°N latitude are combined to diagnose the zonal wave numbers (m) of spectral wave signatures during the Southern Hemisphere sudden stratospheric warming (SSW) 2019. Diagnosed are quasi-10- and 6-day planetary waves (Q10DW and Q6DW, $m = 1$), solar semidiurnal tides with $m = 1$, 2, 3 (SW1, SW2, and SW3), lunar semidiurnal tide, and the upper and lower sidebands (USB and LSB, $m = 1$ and 3) of Q10DW-SW2 nonlinear interactions. We further present 7-year composite analyses to distinguish SSW effects from climatological features. Before (after) the SSW onset, LSB (USB) enhances, accompanied by the enhancing (fading) Q10DW, and a weakening of climatological SW2 maximum. These behaviors are explained in terms of Manley-Rowe relation, that is, the energy goes first from SW2 to Q10DW and LSB, and then from SW2 and Q10DW to USB. Our results illustrate that the interactions can explain most wind variabilities associated with the SSW.

Plain Language Summary Sudden stratospheric warming events occur typically over the winter Arctic and are well known for being accompanied by various tides and Rossby waves. A rare SSW occurred in the Southern Hemisphere in September 2019. Here, we combine mesospheric observations from the Northern Hemisphere to study the wave activities before and during the warming event. A dual-station approach is implemented on high-frequency-resolved spectral peaks to diagnose the horizontal scales of the dominant waves. Diagnosed are multiple tidal components, multiple Rossby normal modes, and two secondary waves arising from nonlinear interactions between a tide component and a Rossby wave. Most of these waves do not occur in a climatological sense and occur around the warming onset. Furthermore, the evolution of these waves can be explained using theoretical energy arguments.

1. Introduction

In the winter polar atmosphere, upward propagating Rossby waves (RWs, also called planetary waves), for example, triggered by topography and the horizontal thermal gradient of the land-sea distribution, may interact with the polar vortex and heat the stratosphere rapidly, leading to phenomena known as sudden stratospheric warming events (SSWs, e.g., Butler et al., 2015). Associated with SSWs are oscillations in the middle and upper atmosphere in both neutral and plasma properties, such as the neutral density and composition, temperature, wind, plasma density, and electric current density (e.g., Goncharenko & Zhang, 2008; Pedatella & Forbes, 2010).

In the mesosphere, planetary-scale oscillations during SSWs can be categorized into two temporal scales, longer and shorter than 1 day, termed hereafter as RW- and tide-like oscillations, respectively. RW-like oscillations occur at periods from a few days to a few tens of days, mostly explained as RW normal modes (RNMs, e.g., Forbes, 1995; Madden, 1979). RNMs are westward propagating and occur with wave periods near 2, 6, 10, 16, and 28 days and are often referred to as quasi-2-, 6-, 10-, 16-, and 28-day waves (Q2DW, Q6DW, Q10DW, Q16DW, and Q28DW, e.g., Forbes et al., 2017, 2020; Yamazaki, 2018). Associations between

RNMs and SSWs have also been broadly reported, although the underlying mechanisms are still under debate (e.g., Pancheva et al., 2008; Stray et al., 2015). Besides RNMs, secondary waves of nonlinear interactions between RNMs and stationary RWs are also observed during SSWs (e.g., He, Forbes, et al., 2020).

Oscillations occurring around the periods of harmonics of the solar or lunar day are explained mostly as signatures of harmonics of solar or lunar tides. Oscillations of this nature are reported to be associated with or impacted by SSWs, such as the first six solar migrating tidal harmonics (He, Yamazaki, et al., 2020), and the second lunar migrating tidal harmonic (M2, e.g., He & Chau, 2019). Among these oscillations, the Sun-synchronous (migrating tide-like) components are typically explained in terms of SSW modulations of tidal heating (e.g., Goncharenko et al., 2012; Siddiqui et al., 2020) and of propagation conditions (e.g., Jin et al., 2012), whereas the non-Sun-synchronous (nonmigrating tide-like) components are conventionally explained as arising from zonal asymmetries in heating or nonlinear interactions between stationary RWs and migrating tides (e.g., Liu et al., 2010). Nonlinear interactions could also occur between RNMs and tides (e.g., Forbes et al., 2020), generating secondary waves at frequencies slightly below and above the tidal frequencies, termed hereafter as lower and upper sidebands (LSBs and USBs), respectively. LSBs and USBs are often misinterpreted as tides (He & Chau, 2019).

Most knowledge of the above mesospheric wave activities is based on SSWs that occurred in the Northern Hemisphere (NH). In September 2019, an SSW occurred (Yamazaki et al., 2020) in the Southern Hemisphere (SH), providing a unique opportunity to investigate the response of the NH middle and upper atmosphere to SH SSWs. Using Aura Microwave Limb Sounder (MLS) observations and Swarm plasma and magnetic observations, Yamazaki et al. (2020) revealed 6-day periodicities in the middle atmosphere and ionosphere. Conventionally, such like periodicities were explained most often as Q6DW. However, a recent modeling study (Miyoshi & Yamazaki, 2020) suggested that the ionospheric 6-day periodicities in the 2019 case might not be Q6DW signatures but aliases from near-12-hr waves that resulted from Q6DW-SW2 nonlinear interaction. This aliasing, between RNWs and their secondary waves associated with migrating tides, is an inherent sampling property of all quasi-Sun-synchronous single-spacecraft missions (see Text S1 in the supporting information, also, cf. Moudden & Forbes, 2014). The current work uses ground-based observations to eliminate the concerns about the aliasing and investigate the potential RNMs and near-12-hr waves. Implementing a dual-station approach, we are also able to diagnose zonal wave numbers of the underlying waves, beyond the capabilities of single-station approaches. Our results illustrate the presence of both RNMs and near-12-hr waves in the mesosphere and reveal how the Q10DW-tidal interactions result in the mesospheric wind variability during the SH SSW.

2. Observation and Method

The current work uses five radar systems, at Juliusruh (13.4°E, 54.6°N), Mohe (122°E, 53.5°N), Andenes (16.0°E, 69.3°N), PokerFlat (147.5°W, 65.1°N), and Yellowknife (114.3°W, 62.5°N), referred hereafter as J, M, A, P, and Y radars, respectively. The details of radar setups, for example, frequencies and antenna configurations, were introduced in Hoffmann et al. (2010), Yu et al. (2013), Singer et al. (2013), Klemm (2019), and Kumar and Hocking (2010), respectively. As illustrated by two dashed lines in Figure S1, these radars are located largely along two latitudes, 65°N and 54°N. The zonal and meridional wind observations (u and v) around the SSW, between 1 June and 31 November 2019 (except at Yellowknife where data are not available before 13 August), are derived between 80- and 100-km altitude for a case study. As a reference and for comparison, 7-year (2012–2018) observations at Mohe and Juliusruh are also used for a composite analysis (CA).

Our main approach is the so-called phase differencing technique (PDT), developed in He, Chau, Stober, et al. (2018) and has been explained mathematically and implemented several times (e.g., He, Chau, Hall, et al., 2018). Here, we explain PDT briefly. Based on dual-point configurations, PDT makes use of the phase difference between two locations on the wave path to estimate the wave number in the direction defined by the two points. When the two locations are at the same latitude, the zonal wave number m can be estimated. The estimation is based on two main assumptions. The first one, called single-wave assumption, is that the wave number is a function of frequency. The other, called long-wave assumption, is that the separation between the two locations is shorter than half the wavelength of the underlying wave, which is used to deal with the wave number aliasing. A dual-radar configuration with longitudinal separation λ_Δ is associated with a Nyquist wave number $m_N = \frac{2\pi}{2\lambda_\Delta}$. Then, for all integers Z and a wave number m_0, the solutions

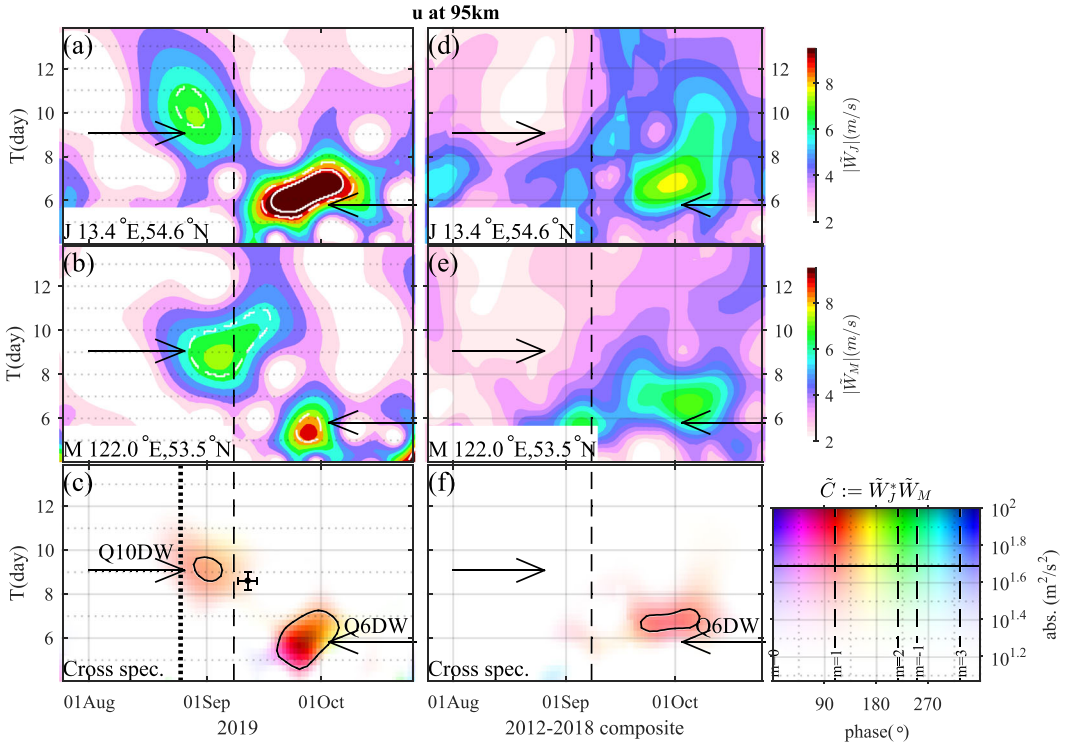

Figure 1. Wavelet spectra of the zonal wind at 95-km altitude over the radar systems at (a) Juliusruh and (b) Mohe, and (c) their cross-wavelet spectrum. In each panel, the vertical dashed line represents the SH SSW onset; the horizontal arrows indicate the periods of the maxima of two peaks in (c). In (a) and (b), the dashed and solid white lines display the 90% and 95% confidence levels, respectively. In (c), the color hue represents the phase difference between (a) and (b); the color hue is adjusted so that the redness denotes exactly $m = 1$; the vertical dotted line is a time reference for comparison with Figure 2c; the black isolines denote the amplitude $\sqrt{|\widetilde{C}|} = 7$ m/s; the horizontal error bar illustrates the temporal distribution of the USB- and LSB-like maxima indicated by the white crosses in Figures 2a–2c, while the vertical bar illustrates the distribution of the estimated periods of RNM that can interact with SW2 and give rise to the maxima. (d–f) The same plots as (a–c) but from composite analyses between 2012 and 2017.

$m = m_0 + Zm_N$ are aliases of each other, as implied in Equation A1 in He, Yamazaki, et al. (2020). Particularly, in diagnosing RWs and tides, m could be assumed as a near-zero integral number, which might relax the long-wave assumption from half wavelength to one and a half wavelength. PDT has been implemented, through cross-wavelet (CWL) analysis, to diagnose m of RW- and tide-like oscillations in a few NH SSWs and validated by comparing results from different dual-station configurations at the same latitude (e.g., He, Forbes, et al., 2020; He, Yamazaki, et al., 2020). The current work applies PDT to the SH SSW 2019, using three dual-radar configurations, that is, M-J, P-A, and Y-A.

3. Results

As explained in section 1, most planetary-scale wave activities during SSWs are RW- and tide-likes oscillations. Therefore, we explore the waves in two frequency ranges in sections 3.1 and 3.2, respectively. Section 3.3 focuses only on $T = 12.0 \pm 0.2$ hr.

3.1. Multiday Oscillations

Figure 1a presents $|\widetilde{W}^J_{(f,t)}|$, a Gabor wavelet (Torrence & Compo, 1998) of the zonal wind at 95-km altitude over Juliusruh. Representing the SSW onset, the dashed vertical line illustrates the central day between 5 and 11 September, during which the atmospheric temperature at 10 hPa increased by 51 K (Yamazaki et al., 2020). The most dominant feature of Figure 1a) is the peak at periods $T = 6$–8 days around 1 October, as highlighted by a horizontal arrow. There is another peak around $T = 10$ days around 1

September, before the onset and highlighted by an arrow. Both of the 6- and 10-day peaks also occurred over Mohe, as displayed in the spectrum $|\widetilde{W}^{M}_{(f,t)}|$ in Figure 1b. The coincidence between the two radars allows the diagnosis of m through CWL analysis (e.g., He, Forbes, et al., 2020). The CWL spectrum between Figures 1a and 1b, $\widetilde{C}_{(f,t)} = \widetilde{W}^{J*}_{(f,t)}\widetilde{W}^{M}_{(f,t)}$, is shown in Figure 1c, in which the darkness and the color hue denote the amplitude $|\widetilde{C}|$ and phase $Arg\left\{\widetilde{C}\right\}$. $Arg\left\{\widetilde{C}\right\}$ measures the phase difference between the stations. Assuming the phase difference is due to the propagation of a dominant wave with the wave number m, then $Arg\left\{\widetilde{C}\right\} = m\lambda_{\Delta}$ is a function of m and the longitudinal separation between the two radars λ_{Δ}. The color hue of Figure 1c is adjusted so that the redness represents $Arg\left\{\widetilde{C}\right\} = \lambda_{\Delta}$, corresponding to $m = 1$. In Figure 1c, both the 6- and 10-day peaks are associated with $m = 1$, suggesting both peaks are the RNMs, that is, Q6DW and Q10DW, respectively. Similar Q6DW and Q10DW signatures occur also at 65°N detected by the P-A radar pair, as displayed in Figure S2d.

For comparison and as a reference, we present a CA in Figures 1d–1f, using the data from the J-M pair between 2012 and 2018. Similarly to the 2019 case, in Figures 1d–1f Q6DW also occurs around 1 October, whereas Q10DW is not visible around 1 September, which is different from the 2019 case. Specifically, for every single year that our data cover, the Q6DW signature occurs in the same season above $\sqrt{|\widetilde{C}|} >= 7$ m/s, suggesting it is a climatological behavior.

3.2. Near-12-hr Oscillations

Figure 2a presents a CWL spectrum similar to Figure 1c but altitude-averaged at periods near 12 hr. Different from Figure 1c which uses only u, Figure 2a sums the spectra of u and v since the spectra are almost identical to each other. The black isolines denote amplitudes at $\sqrt{|\widetilde{C}|} = 8$, 12, 16, and 24 m/s. In Figure 2a, the most dominant peak occurs at 12.0 hr, characterized by $m = 2$ and $\sqrt{|\widetilde{C}|} >$ 24 m/s before the SSW onset, corresponding to the tidal component SW2. In the current work, SWm denotes semidiurnal westward propagating component with zonal wave number m. In Figure 2a and at 12.4 hr, as indicated by a horizontal arrow, another peak occurs above $\sqrt{|\widetilde{C}|} >$ 12 m/s. The 12.4-hr peak is characterized by $m = 2$, and therefore should be a signature of the lunar tide M2.

Figure 2b is the same plot as Figure 2a but from the radar pair A-P, at 65°N. Similarly to Figure 2a, in Figure 2b the spectrum also maximizes at 12.0 and 12.4 hr above $\sqrt{|\widetilde{C}|} >$ 24 and 12 m/s, respectively. The 12.0-hr peak is mostly characterized by $m = 2$, and so is the 12.4-hr peak, which therefore suggests that the underlying waves are SW2 and M2, respectively. In addition, in Figure 2b and between 11.0 and 11.5 hr, there is a dominant blue peak, maximizing at $\sqrt{|\widetilde{C}|} = 17.9$ m/s, at $T = 11.36$ hr on 12 September 2019, as indicated by the white cross. However, the color of the 11.36 hr is close to $m = 1$ and $m = 3$ in the color code map, due to the special radar separation $\lambda_{\Delta} \approx \pi$ and $\lambda_{\Delta}+2\pi \approx 3\lambda_{\Delta}$. To determine m, we produce the same spectra as Figure 2b but for the radar pair A-Y, displayed in Figure 2c.

Similarly to Figure 2b, Figure 2c also exhibits peaks at $T = 12.4$, 12.0, and 11.0–11.5 hr. The previous two are associated with $m = 2$, whereas the third peak, as illustrated by the white cross, maximizes at $\sqrt{|\widetilde{C}|} = 11.1$ m/s, at $T = 11.29$ hr on 14 September 2019. The blueness suggests that the underlying dominant wave is associated with $m = 3$, which is compatible with the blue peak in Figure 2b. Actually, the color codes for all the panels of Figure 2 are adapted so that the blueness represents $m = 3$. A weak blue or purple peak could also be found in Figure 2a as indicated by the white cross, maximizing at $\sqrt{|\widetilde{C}|} = 9.1$ m/s, $T = 11.36$ hr. Additionally, in Figure 2c and immediately before the onset, a red peak occurs at $T = 12.73$ hr with $\sqrt{|\widetilde{C}|} = 8.0$ m/s as indicated by a white cross. The redness suggests that the underlying wave is associated with $m = 1$. Similar 12.7-hr peaks also occur in Figures 2b and 2a, indicated by white crosses there.

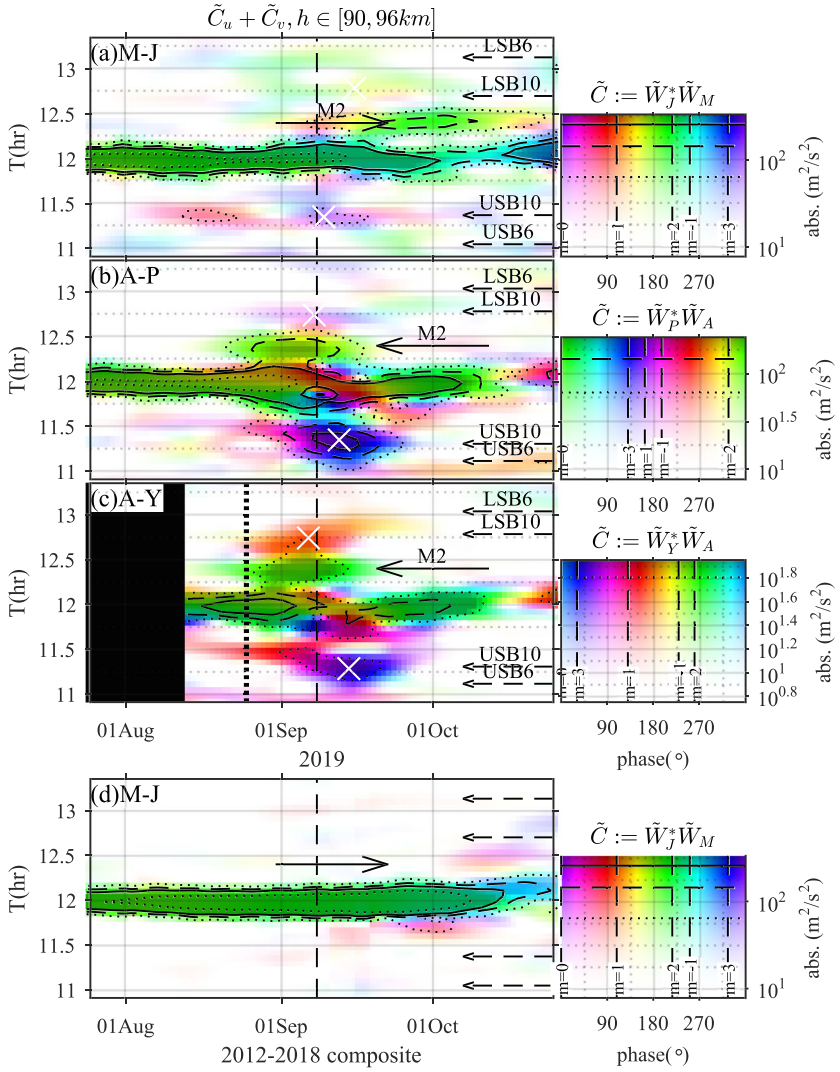

Figure 2. (a) Near-12-hr CWL spectrum for the radar pair M-J, namely, a similar plot as Figure 1c but summing the spectra of the zonal and meridional winds, averaged between 90 and 96 km. All panels are adjusted so that blueness represents $m = 3$. (b, c) Same plots as (a) but for the radar pairs A-P and A-Y, respectively. (d) Same as (a) but for the 2012–2018 composite analysis. In each panel, the black isolines denote amplitudes at $\sqrt{|\tilde{C}|} = 8$, 12, 16, and 24 m/s; the solid horizontal arrow indicates the M2-like signature; the dashed arrows on the rightmostside illustrate the theoretical periods of the secondary waves (USB and LSB) of SW2-Q6DW and SW2-Q10DW nonlinear interactions; and the white crosses indicate local maxima of USB- and LSB-like peaks. Note that here only spectral peaks above the 95% confidence level are discussed in the current work.

Figure 2d displays the same plot as Figure 2a but from the 7-year CA, which comprises mainly the 12.0-hr peak but not the off-12.0-hr peaks seen in Figures 2a–2c, at least not at the comparable magnitudes. The 12.0-hr peak is also different from those in Figures 2a–2c), for example, the peak exhibits a minimum in late October in Figure 2d, but prematurely around 1 October in Figure 2a. We look into the details in the next subsection.

3.3. Solar Semidiurnal Tide

To investigate the 12.0-hr peak, we reproduce spectra similar to Figure 2a but at every individual altitude, and then pick the values only at $T = 12.0 \pm 0.2$ hr at each altitude and combine them into the time-height plane, displayed in Figure 3a. Similarly, Figures 3b–3d are constructed from spectra similar to Figures 2b–2d. In all panels here, green represents $m = 2$. The most dominant feature in Figure 3d is the

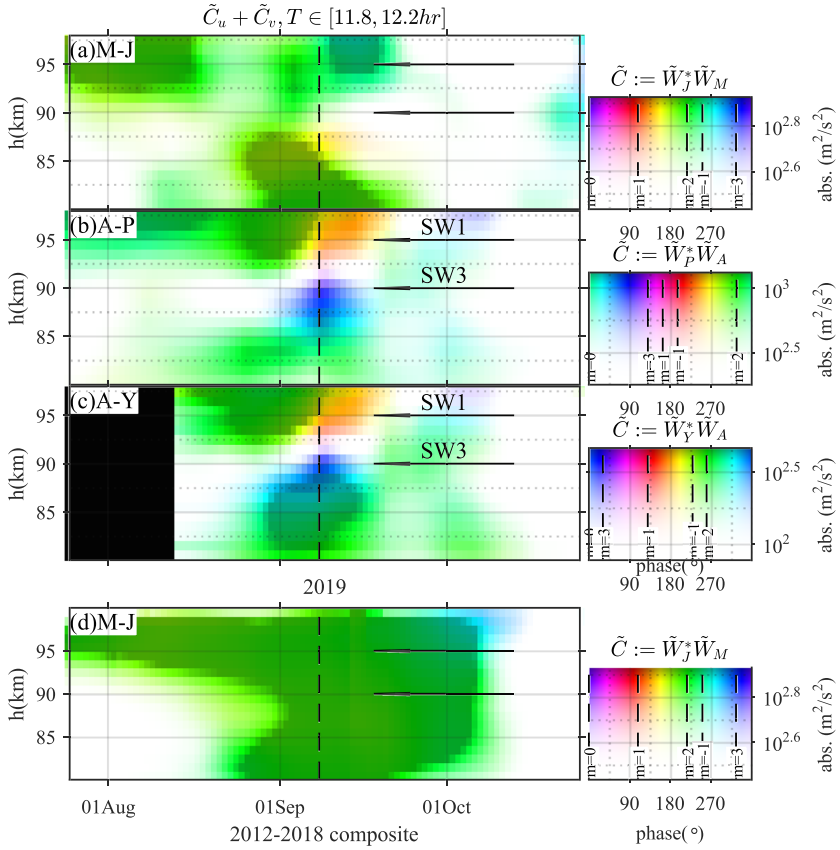

Figure 3. Same variable and panel arrangement as displayed in Figure 2 but as a function of date and altitude only at period $T = 12.0$ hr. for example, panel (a) is combined from similar spectra as Figure 2a but at each individual altitude. The color is adapted so that green represents $m = 2$. In (b) and (c), the horizontal arrows indicate SW1- and SW3-like signatures.

green peak ($m = 2$), maximizing vertically at about 90 km in September. The September maximum is a well-known climatological behavior (Figure 7, He & Chau, 2019). The pattern around the SSW in Figure 3a could be explained as a distorted version of the climatological maximum. The maximum occurs 10-20 days earlier and splits around 90 km and above, in comparison with Figure 3d.

The premature and split maximum also occurs in Figures 3b and 3c, but associated with more interesting behaviors. As indicated by the horizontal arrows, blueness (or purpleness) and redness occur at $h = 90$ and 95 km, respectively. These colors suggest that the dominant underlying wave there is not SW2. In Figure 3c, blueness and redness represent $m = 1$ and 3, suggesting that the underlying waves are the nonmigrating tides, SW1 and SW3, respectively.

4. Discussions

The previous section diagnoses the zonal wave number m of potential waves seen in cross-wavelet spectra, in two ranges of period, namely, multidays and near-12-hr. In the current section, we discuss them as RNMs, tides, and secondary waves of RNM-tide nonlinear interactions.

4.1. Association of RNMs With SH SSW

Although there are observational studies suggesting that SSWs are not associated with RNMs (e.g., Sassi et al., 2012), most observational studies support associations, at least for most NH SSWs (e.g., He, Forbes, et al., 2020; Pancheva et al., 2008; Stray et al., 2015). The burst of Q6DW in late September 2019 was reported by Yamazaki et al. (2020) using geopotential height (GPH) observations from Aura MLS and observations from Swarm. The 2019 Q6DW amplitude, in GPH, was stronger than the 2004–2018 average amplitude,

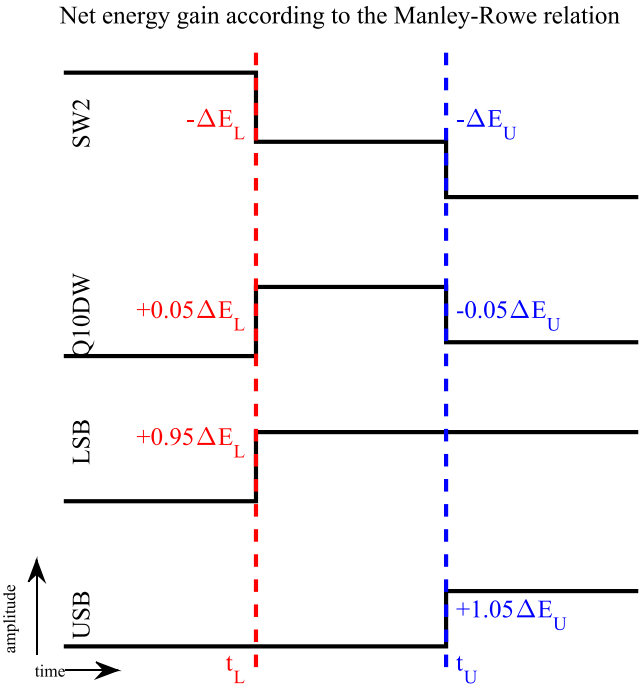

Figure 4. A sketch of the net energy gain of the four waves in the Q10DW-SW2 nonlinear interactions according to the Manley-Rowe relation. The red and blue represent the LSB- and USB-generating interactions occurring at t_L and t_U, respectively. Between t_L and t_U maximizes the Q10DW. ΔE_L and ΔE_U are energy exchanged through SW2. t_L and t_U correspond to the dotted and dashed vertical black lines in Figures 1c and 2c, respectively.

especially above 70-km altitude in SH. Consistently, our comparison between Figures 1c and 1f also illustrates that in NH the 2019 Q6DW is also stronger than the multiyear average. However, such a strong NH Q6DW in this season is not unique for 2019. Among the 7 years we explored, Q6DW also occurred at comparable or even stronger amplitudes in the same season in 2013 and 2017 (observed from the same figures as Figures 1a–1c but for 2012–2018, not shown here).

In contrast to the climatological occurrence of the Q6DW, the occurrence of the Q10DW in early September is unique for 2019, and also temporally more close to the SH SSW, cf. Figures 1a–1c versus 1d–1f. Therefore, we argue that the Q10DW is potentially associated with the SSW. Consistent with our Q10DW results, the SH GPH results (Figure 3a, Yamazaki et al., 2020) exhibited a spectral peak, not mentioned by the authors, at $T = 10$ days around 1 September and weaker than the Q6DW amplitude by at least 50%. The consistency of our NH ground-based results with the SH satellite-based results suggests that the Q6DW and Q10DW are both active on global scales, consistent with their interpretation as RNM. Coincidentally, a Q10DW signature was also reported in the ionosphere during the SH 2002 (Mo & Zhang, 2020).

RNMs prior to NH SSW onsets could be explained in terms of in situ instability (e.g., Pancheva et al., 2008; Siskind et al., 2010), whereas the RNMs which appeared after the NH SSWs are believed to arise from different mechanisms, for example, the zonal asymmetry of gravity wave breaking (e.g., Manney et al., 2008). Therefore, the Q10DW might be attributable to potential in situ instabilities. Supporting this hypothesis is the evolution of the meridional gradient of the quasi-geostrophic potential derived from the MLS GPH observations (Yamazaki et al., 2020). The gradient is necessary for barotropic/baroclinic instability, even though the evolution and the instability were discussed to explain the Q6DW. Another potential mechanism of the Q10DW generation is the planetary wave amplification by stimulated tidal decay (PASTIDE, He et al., 2017) as detailed in the following subsection.

4.2. Secondary Waves of Q10DW-SW2 Nonlinear Interactions

In sections 3.2 and 3.3, we explained the 12.0- and 12.4-hr spectral peaks as solar and lunar tides, respectively. In the current subsection, we discuss other near-12-hr peaks as the upper and lower sidebands (USB and LSB) of nonlinear interactions between SW2 and RNM, respectively.

According to the resonance conditions of wave-wave nonlinear interaction (e.g., He et al., 2017), the frequency and wave number of USB (LSB) are equal to the sum (difference) of their parent waves. Given that the RNMs, Q6DW, Q10DW, and Q16DW, are associated with $m = 1$, all their USBs and LSBs of interactions with SW2 are associated with $m = 3$ and 1, respectively. Observational evidence with constraints of both f and m were reported for the sidebands of Q6DW and Q16DW using either ground-based or satellite observations (e.g., Forbes & Zhang, 2017). As a reference, the theoretical periods of the USBs and LSBs, associated with the RNMs at periods indicated by the arrows in Figures 1c and S1d, are calculated and displayed as the dashed horizontal arrows at the rightmostside in all panels of Figure 2. Further, using the periods at the six white crosses (indexed hereafter as $k = 1,2, ..., 6$) in Figures 2a–2c, we calculate the theoretically required periods of the parent RNMs according to the resonance condition, resulting in six values T_k. Assuming all the six peaks share one parent RNM and using the spectral amplitude $w_k := |\widetilde{C}_k| / <|\widetilde{C}_k|>_k$ in Figure 2, we calculate the weighted average $\overline{T} := <T_k w_k>_k = 8.6$ days with a deviation $\sigma\left(w_k\left(T_k - \overline{T}\right)\right) = 0.4$ days, displayed as a vertical error bar in Figures 1c and S1. The horizontal error bar represents the corresponding weight-averaged time and its deviation, $\overline{t} = 11.1 \pm 2.2$ days after 00:00, on 1 September. In Figures 1c and S1d, the Q10DW peaks, in comparison with the Q6DW, are closer to the black cross in both T and $\overline{T}$ overlaps

the period of the Q10DW peak partially. Therefore, we argue that the Q10DW, rather than Q6DW, is more likely responsible to the sidebands, or at least contributes more.

Moreover, the temporal evolution of the Q10DW peak, together with those of the LSB, USB, and SW2, satisfies the energy requirements of Manley-Rowe relation (He et al., 2017). The relation implies that the LSB and USB are generated in two nonlinear interaction processes. In the LSB-generating interaction, the tide exports energy to both LSB and RNM, while in the USB-generating interaction, both RNM and tide contribute energy to USB. If we assume that the LSB- and USB-generating interactions occur at t_L and t_U as denoted by the vertical dotted and dashed lines in Figures 1c, 2b, and 2c within infinitely small time intervals, the Manley-Rowe relation can explain the bursts of the Q10DW and LSB around t_L as well as the Q10DW weakening and USB burst around t_U (see Figure 4). These bursts are accompanied by the split of the September SW2 maximum as described in section 3.3. According to the Manley-Rowe relation, the absolute net energy gains of the waves are proportional to their frequencies, and 100% and 95% of the energy of the LSB and USB are contributed directly by SW2. Therefore, the energy deficits of SW2 could be responsible for the splitting of the SW2 maximum in Figures 3a–3c.

On the other hand, Q6DW maximized in late September and is, therefore, less likely responsible for the LSB generation that occurred about 20–30 days prior.

5. Summary

The current study explores planetary-scale wave activities in the NH during the SH SSW 2019, using mesospheric winds detected with five meteor radar systems around 54°N and 65°N. We diagnose the zonal wave number m of wave signatures contained in cross-wavelet spectra of the observations from multiple longitudinal sectors. Spectral peaks are diagnosed at $T = 5$–7 days, 8–10 days, 12.0, 12.4, 11.2–11.5, and 12.6–12.8 hr, associated dominantly with $m = 1$, 1, 2, 2, 3, and 1, which are explained as Q6DW, Q10DW, SW2, M2, and USB and LSB of Q10DW-SW2 nonlinear interaction, respectively. As a reference, a 7-year composite analysis is presented, illustrating that the SW2 pattern during the SH SSW could be explained as a premature and split climatological September maximum and that the Q6DW during the SH SSW could be explained as an amplified climatological phenomenon. The detected periods of the Q10DW, LSB, and USB signatures satisfy the resonance conditions of nonlinear interaction. In addition, the temporal variations of the Q10DW, LSB, USB, and SW2, shortly before and after the SSW onset, could be explained in terms of the Manley-Rowe relation of nonlinear interactions. Our results illustrate that the Q10DW-SW2 interactions can explain the details of the mesospheric wind variabilities during the SH SSW 2019.

Data Availability Statement

The hourly wind data from Mohe is provided by the Data Center for Geophysics (http://www.dx.doi.org/10.12197/2020GA016), National Earth System Science Data Sharing Infrastructure at BNOSE (Beijing National Observatory of Space Environment), IGGCAS (Institute of Geology and Geophysics, Chinese Academy of Sciences). The hourly wind from all radars and analyzed data of all Figures are archived at the service RADAR (https://dx.doi.org/10.22000/343).

Acknowledgments

Maosheng He, Jeffrey M. Forbes, Guozhu Li, and PokerFlat meteor radar are supported by the German Research Foundation (Deutsche-Forschungsgemeinschaft, Grant CH1482/1-2), National Science Foundation (NSF) Award (AGS-1630177) to the University of Colorado Boulder, National Natural Science Foundation of China (42020104002), and NSF Grant (AGS-1651464), respectively.

References

Butler, A. H., Seidel, D. J., Hardiman, S. C., Butchart, N., Birner, T., & Match, A. (2015). Defining sudden stratospheric warmings. *Bulletin of the American Meteorological Society*, *96*, 1913–1928. https://doi.org/10.1175/BAMS-D-13-00173.1

Forbes, J. M. (1995). Tidal and planetary waves. *Geophysical Monograph Series*, *87*, 67–87. http://www.agu.org/books/gm/v087/GM087p0067/GM087p0067.shtml, https://doi.org/10.1029/GM087p0067

Forbes, J. M., & Zhang, X. (2017). The quasi-6 day wave and its interactions with solar tides. *Journal of Geophysical Research: Space Physics*, *122*, 4764–4776. https://doi.org/10.1002/2017JA023954

Forbes, J. M., Zhang, X., Hagan, M. E., England, S. L., Liu, G., & Gasperini, F. (2017). On the specification of upward-propagating tides for ICON science investigations. *Space Science Reviews*, *212*, 697–713. https://doi.org/10.1007/s11214-017-0401-5

Forbes, J. M., Zhang, X., & Maute, A. (2020). Planetary wave (PW) generation in the thermosphere driven by the PW-modulated tidal Spectrum. *Journal of Geophysical Research: Space Physics*, *125*, e2019JA027704. https://doi.org/10.1029/2019JA027704

Goncharenko, L. P., Coster, A. J., Plumb, R. A., & Domeisen, D. I. (2012). The potential role of stratospheric ozone in the stratosphere-ionosphere coupling during stratospheric warmings. *Geophysical Research Letters*, *39*, L08101. https://doi.org/10.1029/2012GL051261

Goncharenko, L. P., & Zhang, S. R. (2008). Ionospheric signatures of sudden stratospheric warming: Ion temperature at middle latitude. *Geophysical Research Letters*, *35*, L21103. https://doi.org/10.1029/2008GL035684

He, M., & Chau, J. L. (2019). Mesospheric semidiurnal tides and near-12 h waves through jointly analyzing observations of five specular meteor radars from three longitudinal sectors at boreal midlatitudes. *Atmospheric Chemistry and Physics*, *19*, 5993–6006. https://www.atmos-chem-phys.net/19/5993/2019/acp-19-5993-2019.html

He, M., Chau, J. L., Hall, C. M., Tsutsumi, M., Meek, C., & Hoffmann, P. (2018). The 16-Day planetary wave triggers the SW1-tidal-like signatures during 2009 sudden stratospheric warming. *Geophysical Research Letters*, *45*, 12,631–12,638. https://doi.org/10.1029/2018GL079798

He, M., Chau, J. L., Stober, G., Hall, C. M., Tsutsumi, M., & Hoffmann, P. (2017). Application of Manley-Rowe relation in analyzing nonlinear interactions between planetary waves and the solar semidiurnal tide during 2009 sudden stratospheric warming event. *Journal of Geophysical Research: Space Physics*, *122*, 10,783–10,795. https://doi.org/10.1002/2017JA024630

He, M., Chau, J. L., Stober, G., Li, G., Ning, B., & Hoffmann, P. (2018). Relations between semidiurnal tidal variants through diagnosing the zonal wavenumber using a phase differencing technique based on two ground-based detectors. *Journal of Geophysical Research: Atmospheres*, *123*, 4015–4026. https://doi.org/10.1002/2018JD028400

He, M., Forbes, J. M., Chau, J. L., Li, G., Wan, W., & Korotyshkin, D. V. (2020). High-order solar migrating tides quench at SSW onsets. *Geophysical Research Letters*, *47*, e2019GL086778. https://doi.org/10.1029/2019GL086778

He, M., Yamazaki, Y., Hoffmann, P., Hall, C. M., Tsutsumi, M., Li, G., & Chau, J. L. (2020). Zonal wavenumber diagnosis of Rossby wave like oscillations using paired ground based radars. *Journal of Geophysical Research: Atmospheres*, *125*, e2019JD031599. https://doi.org/10.1029/2019JD031599

Hoffmann, P., Becker, E., Singer, W., & Placke, M. (2010). Seasonal variation of mesospheric waves at northern middle and high latitudes. *Journal of Atmospheric and Solar*, *72*(14), 1068–1079. https://doi.org/10.1016/j.jastp.2010.07.002

Jin, H., Miyoshi, Y., Pancheva, D., Mukhtarov, P., Fujiwara, H., & Shinagawa, H. (2012). Response of migrating tides to the stratospheric sudden warming in 2009 and their effects on the ionosphere studied by a whole atmosphere-ionosphere model GAIA with COSMIC and TIMED/SABER observations. *Journal of Geophysical Research*, *117*, A10323. https://doi.org/10.1029/2012JA017650

Klemm, J. (2019). Classification and signal processing of radio backscatter from meteors, (Master's thesis). University of Alaska Fairbanks. Retrieved from http://hdl.handle.net/11122/10901

Kumar, G. K., & Hocking, W. K. (2010). Climatology of northern polar latitude MLT dynamics: Mean winds and tides. *Annales de Geophysique*, *28*(10), 1859–1876. https://doi.org/10.5194/angeo-28-1859-2010

Liu, H. L., Wang, W., Richmond, A. D., & Roble, R. G. (2010). Ionospheric variability due to planetary waves and tides for solar minimum conditions. *Journal of Geophysical Research*, *115*, A00G01. https://doi.org/10.1029/2009JA015188

Madden, R. A. (1979). Observations of large-scale traveling Rossby waves. *Reviews of Geophysics*, *17*(8), 1935. https://doi.org/10.1029/rg017i008p01935

Manney, G. L., Krüger, K., Pawson, S., Minschwaner, K., Schwartz, M. J., Daffer, W. H., et al. (2008). The evolution of the stratopause during the 2006 major warming: Satellite data and assimilated meteorological analyses. *Journal of Geophysical Research*, *113*, D11115. https://doi.org/10.1029/2007JD009097

Miyoshi, Y., & Yamazaki, Y. (2020). Excitation mechanism of ionospheric 6-day oscillation during the 2019 September sudden stratospheric warming event. *Journal of Geophysical Research: Space Physics*, *125*, e2020JA028283. https://doi.org/10.1029/2020JA028283

Mo, X., & Zhang, D. (2020). Quasi-10-d wave modulation of an equatorial ionization anomaly during the Southern Hemisphere stratospheric warming of 2002. *Annales de Geophysique*, *38*, 9–16. https://doi.org/10.5194/angeo-38-9-2020

Moudden, Y., & Forbes, J. M. (2014). Quasi-two-day wave structure, interannual variability, and tidal interactions during the 2002–2011 decade. *Journal of Geophysical Research: Atmospheres*, *119*, 2241–2260. https://doi.org/10.1002/2013JD020563

Pancheva, D., Mukhtarov, P., Mitchell, N. J., Merzlyakov, E., Smith, A. K., Andonov, B., & Murayama, Y. (2008). Planetary waves in coupling the stratosphere and mesosphere during the major stratospheric warming in 2003/2004. *Journal of Geophysical Research*, *113*, D12105. https://doi.org/10.1029/2007JD009011

Pedatella, N. M., & Forbes, J. M. (2010). Evidence for stratosphere sudden warming-ionosphere coupling due to vertically propagating tides. *Geophysical Research Letters*, *37*, L11104. https://doi.org/10.1029/2010GL043560

Sassi, F., Garcia, R. R., & Hoppel, K. W. (2012). Large-scale Rossby normal modes during some recent Northern Hemisphere winters. *Journal of the Atmospheric Sciences*, *69*(3), 820–839. https://doi.org/10.1175/jas-d-11-0103.1

Siddiqui, T. A., Maute, A., & Pedatella, N. M. (2020). On the importance of interactive ozone chemistry in Earth-system models for studying mesophere-lower thermosphere tidal changes during sudden stratospheric warmings. *Journal of Geophysical Research: Space Physics*, *124*, 10,690–10,707. https://doi.org/10.1029/2019JA027193

Singer, W., Hoffmann, P., Kishore Kumar, G., Mitchell, N. J., & Matthias, V. (2013). Atmospheric coupling by gravity waves: Climatology of gravity wave activity, mesospheric turbulence and their relations to solar activity. In F. J. Lübken (Ed.), *Clim. Weather Sun-Earth Syst*, *highlights from a prior. progr* (pp. 409–427). Dordrecht: Springer Netherlands. https://doi.org/10.1007/978-94-007-4348-9_22

Siskind, D. E., Eckermann, S. D., McCormack, J. P., Coy, L., Hoppel, K. W., & Baker, N. L. (2010). Case studies of the mesospheric response to recent minor, major, and extended stratospheric warmings. *Journal of Geophysical Research*, *115*, D00N03. https://doi.org/10.1029/2010JD014114

Stray, N. H., Orsolini, Y. J., Espy, P. J., Limpasuvan, V., & Hibbins, R. E. (2015). Observations of planetary waves in the mesosphere-lower thermosphere during stratospheric warming events. *Atmospheric Chemistry and Physics*, *15*, 4997–5005. https://doi.org/10.5194/acp-15-4997-2015

Torrence, C., & Compo, G. P. (1998). A practical guide to wavelet analysis. *Bulletin of the American Meteorological Society*, *79*(1), 61–78. https://doi.org/10.1175/1520-0477(1998)079(0061:APGTWA)2.0.CO;2

Yamazaki, Y. (2018). Quasi-6-day wave effects on the equatorial ionization anomaly over a solar cycle. *Journal of Geophysical Research: Space Physics*, *123*, 9881–9892. https://doi.org/10.1029/2018JA026014

Yamazaki, Y., Matthias, V., Miyoshi, Y., Stolle, C., Siddiqui, T., Kervalishvili, G., & Alken, P. (2020). September 2019 Antarctic sudden stratospheric warming: Quasi 6 ay wave burst and ionospheric effects. *Geophysical Research Letters*, *47*, e2019GL086577. https://doi.org/10.1029/2019GL086577

Yu, Y., Wan, W., Ning, B., Liu, L., Wang, Z., Hu, L., & Ren, Z. (2013). Tidal wind mapping from observations of a meteor radar chain in December 2011. *Journal of Geophysical Research: Space Physics*, *118*, 2321–2332. https://doi.org/10.1029/2012JA017976